Yield drag in a two-dimensional foam flow around a circular obstacle: Effect of liquid fraction

C. Raufaste[1,a], B. Dollet[1,b], S. Cox[2], Y. Jiang[3], and F. Graner[1]

[1] Laboratoire de Spectrométrie Physique, BP 87, 38402 St Martin d'Hères Cedex, France[c]
[2] Institute of Mathematical and Physical Sciences, University of Wales Aberystwyth, SY23 3BZ, UK
[3] Theoretical Division, Los Alamos National Laboratory, Los Alamos, NM 87545, USA

Abstract. We study the two-dimensional flow of foams around a circular obstacle within a long channel. In experiments, we confine the foam between liquid and glass surfaces. In simulations, we use a deterministic software, the Surface Evolver, for bubble details and a stochastic one, the extended Potts model, for statistics. We adopt a coherent definition of liquid fraction for all studied systems. We vary it in both experiments and simulations, and determine the yield drag of the foam, that is, the force exerted on the obstacle by the foam flowing at very low velocity. We find that the yield drag is linear over a large range of the ratio of obstacle to bubble size, and is independent of the channel width over a large range. Decreasing the liquid fraction, however, strongly increases the yield drag; we discuss and interpret this dependence.

PACS. 47.57.Bc Complex fluids and colloidal systems: Foams and emulsions – 83.80.Iz Material type: Emulsions and foams

1 Introduction

Multiphase materials such as colloids, emulsions, polymer or surfactant solutions, wet granular systems and suspensions of deformable objects like red blood cells are characterized by a complex mechanical behaviour [1], due to the interaction of their constitutive entities. The concentration is one of the key parameters which control the rheology, determining especially the transition from liquid-like to solid-like properties [2].

Amongst these complex fluids, liquid foams provide a convenient model experimental system for laboratory studies of the interplay between structure, concentration and rheology. This is because the bubbles which constitute the foam's internal structure can be easily visualised and manipulated. The mechanical behaviour of foams is very diverse: they appear elastic, plastic or viscous depending on the deformation and velocity gradient [3,4].

A liquid foam consists of gas bubbles separated by a connected network of liquid boundaries. This liquid phase occupies a fraction Φ of the volume of the foam. The "dry-foam" limit, in which Φ tends to zero, corresponds to polyhedral bubbles separated by thin walls. It is associated

with a divergence of certain contributions to the viscous dissipation [5]. However, the foam's non-dissipative properties (such as surface energy [6], shear modulus or yield stress [7,8]) usually tend to a regular, finite limit when the liquid fraction Φ tends to zero.

The total "yield drag" F_Y^t is the minimal force observed when there exists (or, equivalently, required to create) a movement of the foam relative to an obstacle [9]. It is a global, geometry-dependent quantity directly measurable in experiments and in practical applications of foams, for instance when a foam flows through a porous medium [10], or when one introduces an object into a foam (analogous to sticking one's finger into shaving cream).

In the low-velocity limit (in which viscous dissipation is neglected [11,12]) the total yield drag F_Y^t has two contributions. These are due to the pressure inside the bubbles, denoted F_Y^p, and the network of bubble walls (*i.e.*, soap films with surface tension), F_Y^n. Thus,

$$F_Y^t = F_Y^p + F_Y^n. \tag{1}$$

Here we consider the network contribution F_Y^n and show how it is affected by the liquid content of the foam.

We consider a single layer of equal-area bubbles to facilitate preparation and analysis of experiments, as well as numerical and analytical modelling [13]. Section 2 presents a 2D flow of a quasi-2D foam (a bubble monolayer) around a fixed circular obstacle within a long channel: this is the

---

historical experiment of Stokes, already adapted to foams both in 2D [9,14] and 3D [15–18] flows. We compare them with truly 2D simulations using two physically equivalent but differently optimised software packages (Sect. 3). The simulation methods allow easy variation of the geometrical parameters such as bubble, obstacle and channel size and better control of the bubble area. In Section 4, we discuss the issue of a common, unambiguous definition of liquid fraction for all systems, in theory, experiments and simulations. Section 5 presents our results: we show that the yield drag displays the expected dependence with the bubble, obstacle and channel size, and increases when the liquid fraction Φ decreases. The discussion in Section 6 emphasises that taking into account the effect of liquid fraction allows all data to be plotted on a single master curve and that, although they cover different ranges of Φ, the results of both simulation and experiment are consistent with a simple model.

2 Experimental methods

2.1 Foam channel

Our bulk soap solution is de-ionised water with 1% Teepol, a commercial dish-washing liquid. Its surface tension, measured with the oscillating bubble method (that is, imaging the interface shape), is $\gamma = 26.1 \pm 0.2\,\mathrm{mN\ m^{-1}}$, and its kinematic viscosity, measured with a capillary viscometer, is $1.06 \pm 0.04\,\mathrm{mm^2\ s^{-1}}$.

The experimental set-up [9] confines the foam between a liquid reservoir and a glass lid ("liquid-glass" setup [19]). A 1 m long, $w_c = 10\,\mathrm{cm}$ wide tank is filled with soap solution, leaving below the glass lid a free space of thickness h which we can adjust. We will call this parameter the "foam thickness" for simplicity. At its centre is a circular obstacle of diameter $d_0 = 3$ (Fig. 1) or 4.8 cm. At the entrance to the channel, nitrogen is blown at a computer-controlled flow rate, which varies between 5 and 500 ml min^{-1}. A typical value of the average velocity is 3 mm s^{-1}, for a 3.5 mm thickness and a flow rate of 50 ml min^{-1}.

The resulting foam consists in a horizontal monolayer of bubbles. It exits freely at atmospheric pressure at the open end of the channel, $P = P_{\mathrm{atm}}$. In the absence of the obstacle, it yields a two-dimensional plug flow. With the obstacle present, the flow remains two-dimensional (even though the foam itself is not exactly 2D [19]): there is no vertical component of the velocity.

Due to the presence of the obstacle, there is a velocity gradient. There are many bubble rearrangements (so-called "T1s" or neighbour-swapping events): two three-fold vertices contact, merge and re-separate. We observe well-separated T1s; that is, between two T1s, there is enough time for the foam to relax to an equilibrium state. The present flow is slow enough so that we can extrapolate the results to the low-velocity limit [9], where a comparison with quasi-static calculations and simulations makes sense [20]. (Nevertheless note that this is distinct from the zero-velocity case, that is the absence of flow.) The data
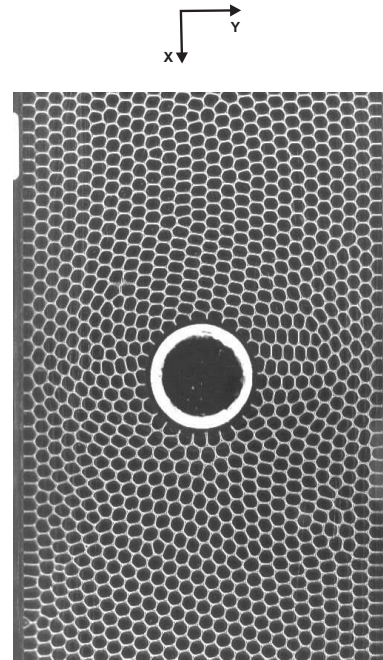

Fig. 1. Image of the experiment, with the foam confined between liquid and glass and flowing from top to bottom. Foam thickness $h = 4.5\,\mathrm{mm}$; bubble area $A = 16\,\mathrm{mm^2}$; obstacle diameter $d_0 = 3\,\mathrm{cm}$; mean velocity $v = 5.6\,\mathrm{mm\ s^{-1}}$; effective liquid fraction $\Phi = 0.06$.

presented below are all in this limit, extracted from the experiments as described in Appendix A.1.

The bubble walls meet the solid boundaries of the foam (glass plate, lateral channel walls, obstacle itself) at a 90° angle [21]. The surface density of bubbles is $1/A$, where A is the average area per bubble (including its walls). The foam is monodisperse: the area variation at the channel entrance is less than 5%. The average area is fixed at a value ranging from $0.121\,\mathrm{cm^2}$ to $0.393\,\mathrm{cm^2}$; most experiments have $A = 0.160\,\mathrm{cm^2}$. Despite the low velocity, and hence the long transit time, we detect neither bubble coalescence nor coarsening. The effect of foam ageing on rheology [22,23] is thus negligible.

2.2 Force measurements

2.2.1 Total yield drag

The obstacle floats just below the top glass surface and is free to move, without solid friction. However, it is linked to a fixed base through a calibrated elastic fibre. We track the obstacle displacement from its position at rest using a CCD camera which images the foam flow from above. We thus measure the force exerted by the flowing foam on the obstacle (precision better than 0.1 mN) [9].

We check that the lift (spanwise component of the resultant force) is consistently zero, within fluctuations, as expected by symmetry (data not shown). After a transient, the total drag F^t (streamwise component of the resultant force) fluctuates around a steady value: we record

the average and standard deviation of these steady-flow data. The extrapolation to the low-velocity limit (or zero-velocity intercept) of the force-velocity curve defines the yield drag F_Y^t. It is independent of the bulk solution viscosity [24], and increases with the obstacle to bubble size ratio [9].

In this paper, we reanalyse the data already published in [9] at various bubble areas, and we present new data for another control parameter: the foam thickness. These data are presented in Appendix A.1. As will be explained in Section 4.2, the foam thickness provides a means by which to vary the liquid fraction in experiments.

2.2.2 Network contribution to the yield drag

We measure F_Y^n as follows. Each bubble wall in contact with the obstacle pulls it with a force equal to its line tension λ (the energy per unit length, which is of order $2\gamma h$, see App. A.2). The elastic contribution of the wall network to the drag is then the vectorial sum of all these individual forces, which all have the same modulus λ. As mentioned above, in a quasi-static flow each wall touches the obstacle at 90° angle. Thus, it suffices to find the contact points between bubble walls and the obstacle and sum all outward normal vectors to the obstacle vectorially at these contact points (which is easy to determine for a circular obstacle). If the downstream geometry of the foam were the same as that upstream, the drag would be zero. Since bubbles are squashed upstream and stretched downstream, the asymmetry means that there are more bubble walls pulling the obstacle downstream, and we measure a downstream elastic contribution to the drag, F_Y^n/λ.

The actual value of the line tension λ is unimportant in what follows, where only measurements of F_Y^n/λ are compared. However, as presented in detail in Appendix A.2, we measure λ to check the consistency of the orders of magnitudes of the independent measurements of F_Y^n and F_Y^t.

3 Simulations

3.1 Deterministic simulations (the Surface Evolver)

The Surface Evolver [25, 26] offers the possibility to reach a true quasi-static limit, that is a succession of exact equilibrium states, through a deterministic minimisation of the foam's energy. It yields precise details of the foam structure.

3.1.1 Preparation of the foam

We use a mode in which all bubble walls are represented as circular arcs. The Surface Evolver lets these circular arcs evolve in order to minimise the total perimeter (equivalent to the energy, up to the prefactor λ). It enforces the constraint that bubble areas A remain fixed and determines the corresponding Lagrange multipliers, namely

each bubble's pressure P. Since we can freely choose the units, we call them "cm" and use bubble size $A = 0.16$ or $0.353 \, \mathrm{cm}^2$, channel width $w_c = 10 \, \mathrm{cm}$, and obstacle diameters $d_0 = 1.5$, 3 and $4.8 \, \mathrm{cm}$, to reproduce actual experiments.

The lateral sides of the channel are rigid and do not interact with the foam, ensuring free-slip boundary conditions for the flow, resulting in a 90° angle where a bubble wall meets the side. We adopt a periodic boundary condition in the direction of motion: bubbles that exit at the end of the channel are fed back into the entrance of the channel. We stop the simulation when each bubble has passed the obstacle no more than once.

We begin with a rectangular lattice of 30×25 monodisperse bubbles of area slightly larger than the required area A. We randomly perturb this lattice so that all the unstable fourfold vertices dissociate into pairs of threefold vertices and the whole foam structure relaxes towards equilibrium. We then choose one bubble to be the circular obstacle, and slowly increase its area to the required value (and correspondingly reduce the bubble areas to A) and constrain its edges to lie on a circle. The centre of the circular obstacle is then moved to the centre of the channel and the structure again relaxed to equilibrium.

3.1.2 Simulation of the flow

With the obstacle in the desired location and the foam close to equilibrium, we start the quasi-static iteration procedure. This requires that we move the foam past the obstacle, in a direction which we denote by x; the difficulty is in doing this with the periodic boundary conditions without fixing any vertices or bubble shapes. Our method is to choose a continuous line of consecutive bubble walls from one side of the channel to the other. Joining this to a line at $x = 0$ with lines along the channel walls defines a plane region with a certain area, which we constrain. At each iteration we choose a convenient line of consecutive walls, and increment the target area of the region by a small amount dA (equal to $0.05 \, \mathrm{cm}^2$ in all simulations), resulting in a slight movement of a line of films without modifications to the bubble areas. The total perimeter of the structure is then reduced until it converges to a constant value (Fig. 2a), so that measurements can be performed.

We have double-precision values for the network geometry. We measure the network contribution F_Y^n to the yield drag as in experiments (Sect. 2.2.2). It is the sum of the unit vectors of the bubble wall with one end attached to the obstacle, expressed in units of the line tension (hence as a dimensionless number). Here too, we check that the lift is consistently zero within fluctuations (data not shown).

With the area increment $dA = 0.05 \, \mathrm{cm}^2$, the transient lasts for about 600 iteration steps (Fig. 3a). This is comparable to, but still smaller than, the total simulation time that is reasonably accessible. After this transient, the drag fluctuates around a steady value. Such fluctuations, due to the rearrangements of the bubbles, recall the stress drops
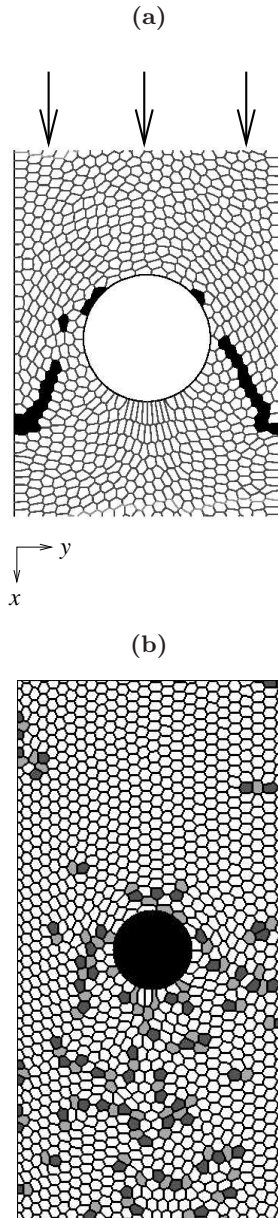
(a)

(b)

Fig. 2. Images of simulated foam flow. The x-axis is parallel to the flow along the channel, with periodic boundary conditions (exiting bubbles re-enter); axis y is spanwise, with free-slip rigid boundary conditions on either side of the channel. (a) Surface Evolver. The image shows the whole simulation domain of 750 bubbles; the shaded bubbles started in a horizontal line. Here $d_0 = 4.8\,\mathrm{cm}$, $A = 0.16\,\mathrm{cm^2}$, $w_c = 10\,\mathrm{cm}$, $L_c = 0.05\,\mathrm{cm}$ and therefore $\Phi = 0.0037$. (b) Potts model. The image shows the simulated channel's full width (except for a few pixels) of 256 pix, and half its length. Here $d_0 = 74\,\mathrm{pix}$, $A = 100\,\mathrm{pix^2}$ and $\Phi = 0.005$. Bubbles coloured in white are without topological defect: 6-sided bulk bubbles, or 5-sided bubbles touching a lateral wall or the obstacle [6]. Bubbles with fewer neighbours are in dark grey, bubbles with more neighbours are in light grey.

observed in Couette experiments for disordered foams [27, 28]. We record the average and standard deviation of these plateaus (steady-flow) data for a total of $1500 - 600 = 900$ iterations. To validate the choice of our simulation size, we
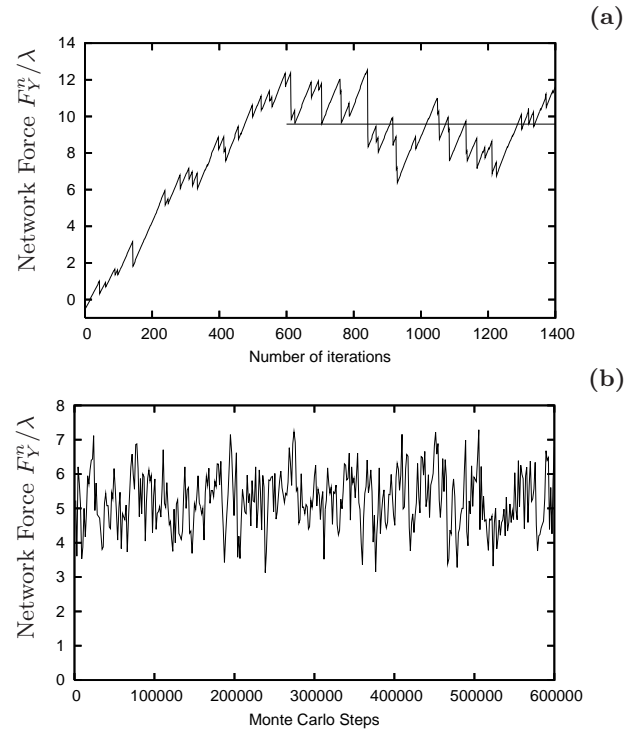
(a)

(b)

Fig. 3. The network force F_Y^n (expressed in units of the line tension λ) measured in simulations *versus* time. (a) Surface Evolver data plotted every iteration step; $d_0 = 4.8\,\mathrm{cm}$, $A = 0.16\,\mathrm{cm^2}$ and $L_c = 0.05\,\mathrm{cm}$, $\Phi = 0.004$. The plateau value is $F_Y^n = 9.6 \pm 1.4$. (b) Potts model data plotted every 1500 Monte Carlo Steps; $d_0 = 74\,\mathrm{pix}$, $A = 100\,\mathrm{pix^2}$, $\Phi = 0.005$. The plateau value is $F_Y^n = 5.4 \pm 1.1$.

checked once that the drag forces are the same with more bubbles in the direction of flow (1250 bubbles instead of 750), although the transient is longer.

Each simulation takes about 35 hours on a Pentium IV 3.20 GHz processor: typically a several-hour build-up to the initial structure (inflating the obstacle), plus one iteration per minute (depending on the number of bubbles and on the liquid fraction).

3.2 Stochastic simulations (Potts model)

To simulate a larger number of bubbles, the Potts model adapted for foam rheology [29] also minimises the same energy, but stochastically (Monte Carlo), which increases the simulation speed. It thus provides more statistics on F_Y^n and allows quicker variation of the geometrical parameters.

3.2.1 Principle of the Potts model

The Potts model is derived from a large-Q Potts model run at zero temperature, a model widely used to model grains in crystals [30]. It has been also applied to different domains of foam physics, including rheology, by enforcing

the conservation of bubble size and applying an external force [29].

We consider a 2D square lattice. Each site i has an integer index σ_i. The k-th bubble is defined as the domain consisting of all sites with the same index value $\sigma_i = k$. Thus, bubbles tile the plane without gaps or overlaps. The evolution is driven by the minimisation of a total energy $\mathcal{H}$ (strictly speaking, it is a Hamiltonian), which has the same three physical ingredients as in the Surface Evolver: interfacial energy, area constraints, external forcing of the flow. Since the calculations are performed on a lattice, we have

$$\mathcal{H} = \lambda \sum_{i,j \text{ neighbours}} [1 - \delta(\sigma_i, \sigma_j)]$$
$$+ \chi \sum_{\text{bubbles } k} \left(A_k - A_k^t\right)^2 + b \sum_{\text{sites } i} x_i. \qquad (2)$$

The first term represents the contribution of the energy of the interfaces between the bubbles. Minimising this term leads to perimeter minimisation. Here δ is the Kronecker symbol: $1 - \delta$ is equal to 1 if the neighbouring sites i, j belong to different bubbles ($\sigma_i \neq \sigma_j$); else it equals zero. We choose to evaluate this term with the fourth-nearest-neighbour interactions to obtain an isotropic line tension insensitive to the details of the lattice [31].

The second term keeps each bubble area A_k (the number of sites with the same index) close to its predefined target value A_k^t. Here χ is the compressibility, which we choose to be high enough to keep bubble areas constant to within a few pixels. The balance between this term and the preceding one simulates a foam relaxing towards mechanical equilibrium.

The third term is a bias term that describes an energy gradient, hence a homogeneous external force field. Here b is the bias intensity and x the site's coordinate along the flow. Without obstacle, the resulting velocity profile would be a plug flow.

We use a Metropolis algorithm to evolve the foam: we randomly select a site at a bubble boundary, change its index to the value of a neighbour if and only if this decreases the total energy (Eq. (2)). Several independent changes are tried successively; a Monte Carlo Step (MCS) is defined conventionally as a number of tries equal to the total number of lattice sites.

3.2.2 Simulation of the flow

As for the Surface Evolver (Sect. 3.1.1), we choose a periodic boundary condition in the direction of flow and free-slip rigid boundary conditions on the channel sides. To ensure that it does not affect the steady-state measurements presented below, the total channel length is $4w_c$, out of which only $2w_c$ are used for measurements and are shown in Figure 2b.

To match the experiments, we choose $16 \leq d_0 \leq 148 \text{ pix}$, $64 \leq A \leq 400 \text{ pix}^2$ and $64 < w_c < 512 \text{ pix}$. Initially, we insert a rigid round obstacle in the centre of the channel, and let a perfectly ordered foam (honeycomb pattern) flow in. We then switch off the bias term by setting $b = 0$, and relax the foam to ensure that the bubbles recover their (near) equilibrium state. The foam has reached the stationary state at the end of this preparation.

We then switch the bias on again, and use the smallest bias b for which the foam flows, which is constant and independent of parameters such as the bubble diameter. We perform measurements at intervals of 1500 MCS (during which a bubble moves a few pixels).

We measure the network contribution to the drag using the same method as in the experiments and Surface Evolver simulations. It fluctuates around a steady value: we record the average and standard deviation of these plateaus (steady-flow) data (Fig. 3b). We run each simulation for a total of 600000 MCS, during which a bubble passes completely through the channel but no bubble passes the obstacle twice. One simulation takes about 12 hours on a Pentium IV 2.8 GHz processor.

4 Liquid fraction

In ideal 2D foams (Sect. 4.1), given A, the liquid fraction scales as the square of the vertex radius. This radius in turn relates to a cut-off length L_c, that is the length at which a bubble edge becomes unstable and the surrounding bubbles undergo a T1. This length L_c is always defined, and is relevant to the mechanical properties investigated here. In experiments, L_c depends on the actual (3D) shape of bubbles; in simulations, L_c is an input parameter.

It suggests a *coherent* definition of the *effective* liquid fraction, presented below, consistent within and between experiments, simulations and theory. Note that we consider here a foam dry enough to have a non-zero shear modulus [32], that is, below the critical liquid fraction [7] (see Eq. (8) for the honeycomb value).

4.1 Ideal 2D foams

In an ideal 2D foam, a Plateau border is a triangle with concave edges of radius R which match tangentially three straight lines meeting at 120° (Fig. 4). The area A_{PB} of a Plateau border is [3]

$$A_{PB} = \left(\sqrt{3} - \frac{\pi}{2}\right) R^2. \qquad (3)$$

The liquid fraction Φ is defined as

$$A_l = A\Phi, \qquad (4)$$

where A_l is the area occupied by the liquid. Since each bubble has n Plateau borders, each being shared among 3 bubbles, we have $A_l = nA_{BP}/3$. For a honeycomb array of bubbles, $n = 6$ and

$$\Phi = \left(2\sqrt{3} - \pi\right) \frac{R^2}{A}. \qquad (5)$$

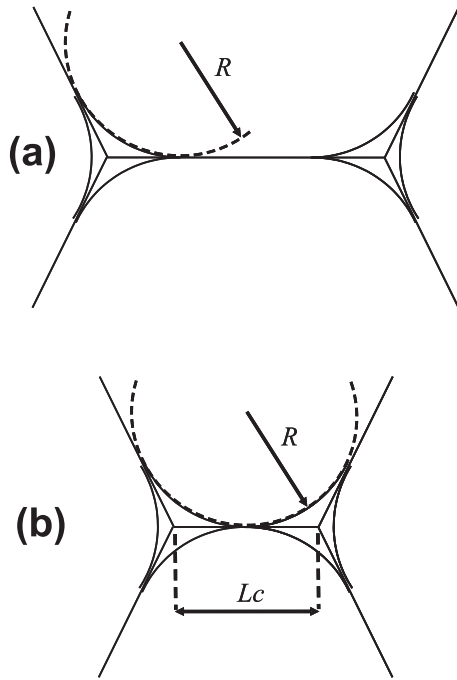Here we consider foams where bubbles have the same area (monodisperse foams), but not necessarily the same

Fig. 4. Picture of two adjacent threefold vertices with Plateau borders. (a) We apply the decoration theorem [32] to model a wet foam. The liquid is present only at the vertices, and (assuming here straight or nearly straight walls) the uniformity of pressure P inside bubbles forces each gas/liquid interface to have the same radius of curvature, R. (b) Critical position of the vertices just before the "T1" neighbour-swapping event. It defines the cut-off wall length L_c.

number of sides n (topological disorder). Since on average over the whole foam $\bar{n} \approx 6$ [3], and since Plateau borders have almost the same size and radius of curvature, equation (5) still holds here approximately.

A T1 is triggered when the distance between these vertices becomes smaller than a cut-off wall length L_c, which increases with R, and thus with Φ. To make this observation more quantitative, one possible convention to define L_c is the condition that two vertices touch (Fig. 4):

$$\frac{R}{\sqrt{3}} = \frac{L_c}{2} , \qquad (6)$$

so that, together with equation (5)

$$\Phi = \frac{3}{2}\left(\sqrt{3} - \frac{\pi}{2}\right)\frac{L_c^2}{A} \approx 0.242 \, \frac{L_c^2}{A}. \qquad (7)$$

Given A, the physical information conveyed by R, Φ or L_c is the same. For comparison between different experiments or simulations, we use Φ because it is dimensionless.

For an ideal honeycomb without shear, all vertices merge at the same liquid fraction: the hexagons become circular when L_c equals the side-length of the hexagons; the bubbles are circular, with a radius equal to R. This critical liquid fraction is [7]

$$\Phi_c = 1 - \frac{\pi}{2\sqrt{3}} = 0.0931. \qquad (8)$$

4.2 Experiments

In the experiments, the actual (3D) shape of bubbles is determined by the foam thickness. Figure 1 shows a foam thickness of 4.5 mm; beyond this thickness, the bubbles undergo a three-dimensional instability and the foam is no longer a monolayer [33]. At the other extreme, at 2 mm and below, the bubbles are circular and separated: both the foam's 2D shear modulus and the yield drag vanish. When h increases, L_c decreases, thus Φ decreases too (Fig. 9 in App. A).

We show in Appendix B that there is a correspondence between L_c and the length $L_{\max}$ of the edge of a bubble just attached to the obstacle (Fig. 11c in App. B). Since $L_{\max}$ is much bigger than L_c, it can be estimated with much more precision in experiment (the uncertainty in both L_c and $L_{\max}$ is one pixel).

We measure on the skeletonized image the length $L_{\max}$ several times preceding its disappearance during a T1 process, and keep the average as $L_{\max}$ and the standard deviation as $\delta L_{\max}^{\mathrm{disp}}$. The skeletonization itself induces a systematic error in determining the actual position of the vertex centre; we estimate as $\delta L_{\max}^{\mathrm{skel}} = 1$ pixel the systematic error on $L_{\max}$. The total uncertainty on $L_{\max}$ is therefore $\delta L_{\max} = \sqrt{(\delta L_{\max}^{\mathrm{disp}})^2 + (\delta L_{\max}^{\mathrm{skel}})^2}$.

To deduce Φ from the measurements of $L_{\max}$, we combine equations (5) and (B.3) to get the following expression as a function of $L_{\max}^2/A$ only:

$$\Phi = \frac{3}{2}\frac{2\sqrt{3} - \pi}{2 + \sqrt{3}}\left(\frac{\sqrt{A}}{L_{\max}} - \frac{L_{\max}}{4\sqrt{3A}}\right)^2. \qquad (9)$$

Its uncertainty is

$$\frac{\delta\Phi}{\Phi} = 2\,\frac{\delta L_{\max}}{L_{\max}}\frac{\sqrt{A}/L_{\max} + L_{\max}/4\sqrt{3A}}{\sqrt{A}/L_{\max} - L_{\max}/4\sqrt{3A}}.$$

4.3 Simulations

The Surface Evolver requires that we specify explicitly the cut-off wall length L_c at which two threefold vertices are allowed to contact, merge and re-separate. Since L_c is an input parameter, it is determined without uncertainty. This defines explicitly an effective liquid fraction (Eq. (7)), at least for small values of Φ. We choose L_c to be of the order of 0.1 cm or slightly smaller, reaching $\Phi = 0.0015$, 0.0037, 0.0061 and 0.015. At very small values of $\Phi < 6\,10^{-6}$, films behind the obstacle would get very stretched and lead to numerical problems. Attempting larger values of $\Phi > 0.015$ would lead to poor convergence in the Surface Evolver and would require that we simulate the actual geometry of the liquid in the vertices (including 4-fold vertices).

In the Potts model, the cut-off distance L_c at which two vertices merge is either 1 or 2 pixels. We use this range to define the uncertainty on the value of Φ. Since we will plot the results in log scale, we choose $L_c \approx \sqrt{2}$ and $\Phi \approx 0.242 \times 2/A \approx 0.5 A^{-1}$ to lie in the middle of this

interval. Thus, the area A of bubbles (that is, the number of pixels per bubble) defines an effective liquid fraction, at least for small values of Φ. The simulated range $64\,\text{pix}^2 \leq A \leq 400\,\text{pix}^2$ corresponds to $0.00125 < \Phi < 0.0075$, large enough to describe realistically the shape of bubbles, and small enough to keep the computation time reasonable.

5 Results

The experiments and both simulations present qualitatively similar images (Figs. 1, 2) and consistent results for the yield drag force, always directed downstream.

There are *a priori* four lengths in this problem: the channel width w_c, the obstacle diameter d_0, the bubble size $\sqrt{A}$; and the cut-off length L_c. As far as we can tell, it is safe to assume that the channel length (if long enough) is irrelevant here. These four lengths can be reduced to three dimensionless parameters. We present the results using: d_0/w_c which characterises the flow geometry; $d_0/\sqrt{A}$ which describes the foam-obstacle interaction; and L_c^2/A which characterises the threshold for T1 rearrangements, and corresponds to the liquid fraction Φ.

5.1 Effect of obstacle to channel size ratio

Potts model simulations indicate that the network yield drag is independent of the ratio of obstacle size to channel width, d_0/w_c (Fig. 5a). This ceases to be valid at small d_0, when the obstacle is comparable in size to a bubble, and at large d_0, when the distance between the obstacle and the channel side is small [26].
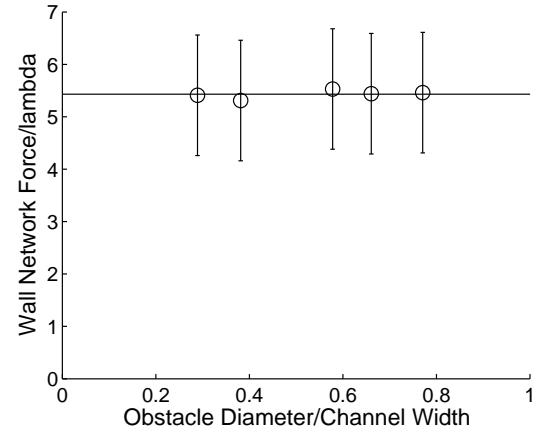
The lack of dependence on d_0/w_c that we find characterises the yielding behaviour of the foam: it means that only a small region near the obstacle is affected by the flow [16]. Nonetheless, the zone where the obstacle influences the flow is larger in 2D [34] than in 3D [16], as elastic or hydrodynamic interactions would suggest.
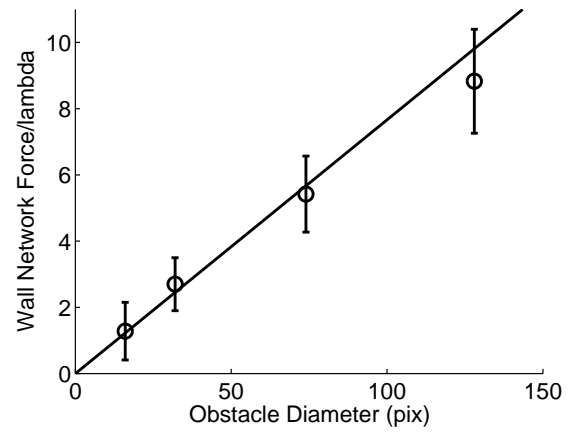
5.2 Effect of obstacle to bubble size ratio

Potts model simulations indicate that the network yield drag increases linearly with the obstacle size d_0 (Fig. 5b) at fixed bubble area. This is consistent with the force increasing as $d_0/\sqrt{A}$, also suggested by the available Surface Evolver data, as well as by experimental measurements of the total force that show the role of the obstacle's spanwise dimension ("leading edge") [9]. Note that most elastic properties of a foam scale as $1/\sqrt{A}$ [3]. In fact, when A increases, the density of bubbles and of bubble walls decreases, and so does the foam's elastic modulus (it would eventually vanish if there were only one large bubble left).

5.3 Effect of liquid fraction

We need to separate the effects of foam geometry, $d_0/\sqrt{A}$, from those of liquid fraction, Φ. We thus rescale the network contribution to the yield drag F_Y^n by $d_0/\sqrt{A}$, and

(a)

(b)

Fig. 5. Network contribution to the yield drag F_Y^n (expressed in units of λ), measured in Potts model simulations with $A = 100\,\text{pix}^2$ ($\Phi = 0.005$). (a) F_Y^n *versus* w_c, for $d_0 = 74$ pix; the solid line is the average (value 5.43). (b) F_Y^n *versus* d_0, for $w_c = 256$ pix; the solid line is a linear fit with zero intercept, $F_Y^n = 0.77\, d_0/\sqrt{A}$.

plot all our data as a function of Φ. All the data, from both experiments and simulations, are well rescaled in the range $10^{-3} < \Phi < 10^{-1}$ (Fig. 6). This is the main result of the present paper.

6 Discussion

6.1 Model

The effect of the liquid fraction on the network drag can be understood as follows. A bubble of area A detaches from the obstacle when its width is of order L_c, and thus its length is of order A/L_c. When Φ decreases, L_c decreases too. Bubbles stretch more downstream, and more bubbles pack behind the obstacle. The number of bubble
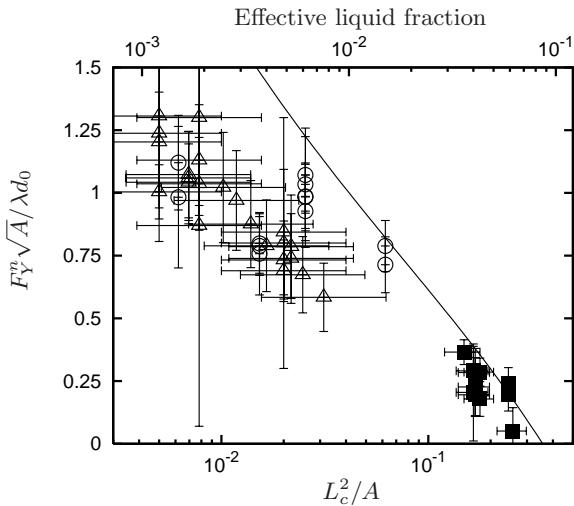
Fig. 6. The network contribution to the yield drag F_Y^n, rescaled by $\lambda d_0/\sqrt{A}$, is plotted *versus* the dimensionless quantity L_c^2/A (bottom scale), that is *versus* the effective liquid fraction Φ (top scale), in the range $10^{-3} < \Phi < 10^{-1}$. All control parameters (d_0, w_c, A and Φ) are varied. Vertical bars indicate the standard deviation of the force fluctuations in time around the plateau value. Horizontal bars indicate the uncertainty discussed in Section 4. Data are from experiments (■), Surface Evolver (○) and Potts model (△); the solid line denotes the analytical model, from equation (B.10), without adjustable parameters. Note that the horizontal scales are logarithmic and shifted with respect to each other.

walls pulling the obstacle downstream increases; simultaneously, the number of walls upstream decreases. This larger up/downstream asymmetry results in an increase in the resulting drag F_Y^n. The contribution from the network (or bubble walls) increases as their number per unit length along the obstacle boundary, namely L_c^{-1}, and thus scales as $1/\sqrt{\Phi}$.

However, the length of the region on which stretched bubbles act decreases, and the divergence in $1/\sqrt{\Phi}$ is in fact softened by a geometrical factor. As shown in Appendix B, we can estimate this factor by integrating the bubble wall contribution around the obstacle. When Φ increases, F_Y^n decreases; it vanishes for $\Phi = 0.086$. This is close to the rigidity loss value (Eq. (8)). Equation (B.10) is plotted in Figure 6, without adjustable parameters. It shows qualitative agreement with the data over two decades of liquid fraction, suggesting that it captures the essence of the physics.

6.2 Influence of the control parameters

In the limit of low Φ, the development of the above argument indicates that, provided that the obstacle diameter and the obstacle-wall distances are larger than the bubble diameter, F_Y^n increases according to

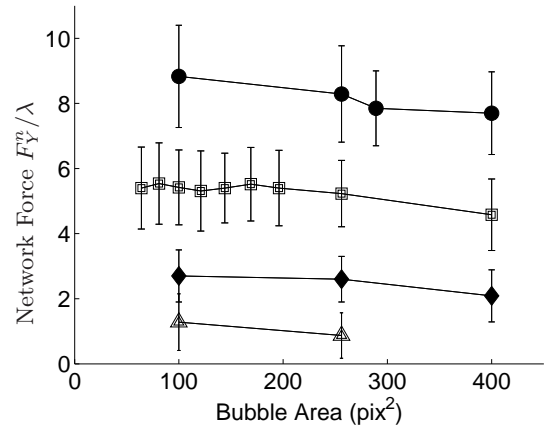$$F_Y^n = \frac{0.516}{\Phi^{1/4}} \frac{\lambda \, d_0}{\sqrt{A}}. \tag{10}$$

Fig. 7. Opposite effects in simulations of F_Y^n (here with Potts model). When A/L_c^2 increases, both $d_0/\sqrt{A}$ and $\Phi \approx A^{-1}$ decrease; so that F_Y^n barely varies (Eq. (10)). Obstacle diameter d_0 equal to 16 (△), 32 (◆), 74 (□) and 128 (●).

In simulations, if we multiply the bubble and obstacle diameters, expressed in units of the cut-off length, by the same prefactor, the network drag changes (data not shown), due to the change in Φ.

Conversely, increasing only the bubble area A at fixed L_c simultaneously decreases both $d_0/\sqrt{A}$ and Φ. This has two opposite effects, the former decreasing F_Y^n, the latter increasing it, resulting in an almost constant F_Y^n (Fig. 7). (In fact there is a weak dependence on area, varying as $A^{-1/4}$.) This shows that the relevant way to vary the liquid fraction in simulations is to modify L_c^2/A at given $d_0/\sqrt{A}$.

6.3 Saturation at low Φ

Surface Evolver simulations allow us to probe the range $10^{-5} < \Phi < 10^{-3}$. They indicate that the force saturates below $\Phi \sim 10^{-3}$, in agreement with our preliminary experiments of a foam confined between glass plates (data not shown).

Direct observation of simulation images of very dry foams (Fig. 8) confirms that the up/downstream asymmetry in the number of bubbles touching the obstacle is around 10, roughly independent of liquid fraction.

The model seems to correctly describe the squashing and stretching of bubble shapes. However, the interpolation between both extreme values assumes a phenomenological expression (Eq. (B.4)). It seems approximately valid only for $10^{-3} < \Phi < 10^{-1}$ (see App. B). It applies to other obstacle shapes, such as an ellipse [35].

6.4 Yield drag versus yield stress

Princen and Kiss [36] have shown that in three dimensions a foam's yield stress scales as $\sigma_Y = \gamma(1 - \Phi_{3D})^{1/3} Y(\Phi_{3D})/R_{32}$, where R_{32} is the surface-volume
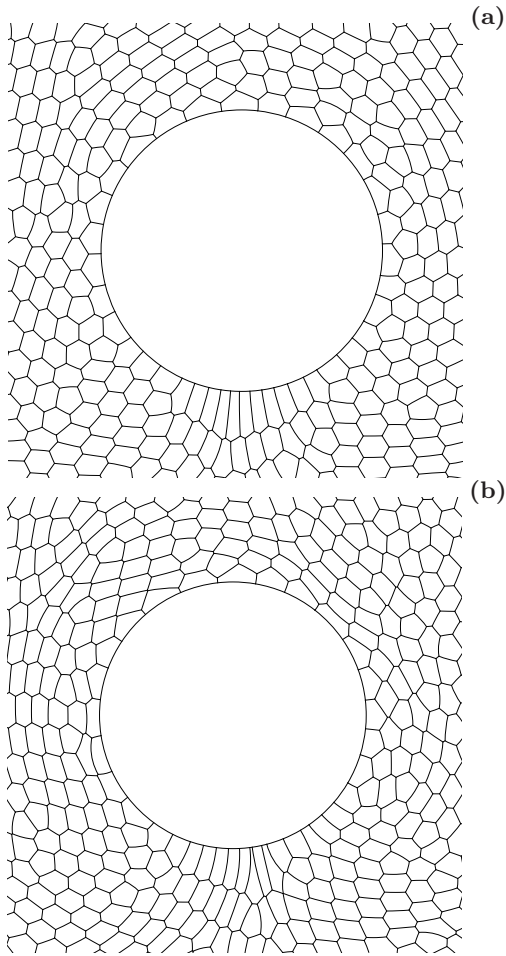
Fig. 8. Surface Evolver simulation of a very dry foam: zoom around the obstacle. (a) $\Phi = 3.7 \ 10^{-3}$; (b) $\Phi = 6 \ 10^{-6}$. Here $d_0 = 4.8 \, \text{cm}$, $A = 0.16 \, \text{cm}^2$, $w_c = 10 \, \text{cm}$. Flow from top to bottom.

mean radius (Sauter radius), and $Y(\Phi_{3D})$ a decreasing function of Φ_{3D} which is approximately $Y(\Phi_{3D}) \simeq -0.080 - 0.114 \ln \Phi_{3D}$ [36].

At this stage, it is worth discussing the fundamental differences between yield stress and yield drag.

The yield stress or yield strain are intrinsic properties of the foam. On the other hand, the yield drag depends on the geometry of the flow: the foam does not yield *everywhere* around the obstacle, and especially not at angles $|\theta| \approx \pi/4$ from the downstream direction, as appears both in experiments (Fig. 1) and in simulations (Figs. 2 and 8). This spatial dependence implies that the relation between yield stress and yield drag is non-trivial and Φ-dependent. In particular, in a dryer foam (Fig. 8), the region where bubbles reach their maximal deformation is narrower [34].

Moreover, the flow around an obstacle involves not only shear, but also elongation, especially near the front and back of the obstacle. When Φ decreases, the bubble elongation can become arbitrary large and dominates the contribution to the yield drag.

7 Conclusion

To summarise, we investigate the two-dimensional flow of a foam around a circular obstacle, within a long channel. Our deterministic (Surface Evolver) and stochastic (Potts model) simulations, as well as our model and experiments, complement and validate each other.

The yield drag is defined as the low-velocity limit of the interaction force between an obstacle and a flowing foam. The network contribution scales as the ratio of obstacle to bubble diameter, as long as this ratio is larger than unity, and is almost independent of the channel width. It increases (because more and more stretched bubbles accumulate behind the obstacle) as a power law when the liquid fraction contained in the foam decreases to 10^{-3}, then saturates.

Having found a relevant definition of the liquid fraction, which is appropriate for experiments, simulations and theory, the dependence of the yield drag with liquid fraction is well characterized. It is very different from that of local intrinsic properties such as the yield stress or shear modulus. This observation suggests that it will be difficult to deduce one quantity from the other. This should be kept in mind in future simulations, and has to be taken into account when modelling the foam behaviour.

Note that this definition of liquid fraction can be extended to other 2D flows in experiments (quasi-2D foam set-ups [19]) or simulations. Extension to 3D [15,16] should also be simple, especially since the main effect of quasi-2D set-ups —external friction on the glass plate [37, 38]— does not seem dominant here. Our present effective liquid fraction based on rheological properties (T1s) facilitates the comparison between 2D and 3D flows (which is difficult when using the actual volume fraction of water [12]). In simulations too, our definition immediately extends to 3D for both Surface Evolver, which uses as input parameter the cut-off area for a face which undergoes a T1; and Potts model, where the voxel (3D pixel) size plays the same role.

Appendix A. Force measurements in experiments

Appendix A.1. Variation with foam thickness

We present here new data concerning the drag exerted by a flowing foam of bubble area $A = 16.0 \, \text{mm}^2$ on a circular obstacle of diameter $d_0 = 3 \, \text{cm}$. We measured the drag, as

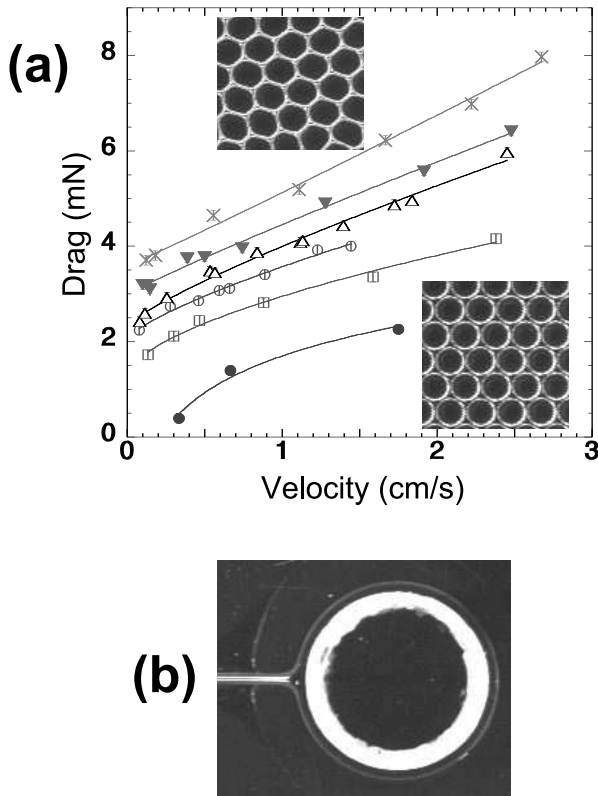**Fig. 9.** (a) Drag *versus* velocity for various distances h between the top plate and the bottom solution: 2.0 (●), 2.5 (□), 3.0 (○), 3.5 (△), 4.0 (▼) and 4.5 mm (×). Here $A = 16.0\,\mathrm{mm}^2$ and $d_0 = 3\,\mathrm{cm}$. The curves are the best fits by the formula $F = F_Y^t + A \times V^a$. Snapshots of the foam of the smallest (bottom) and highest (top) h are also displayed. (b) Photograph of a single soap film pulling on the left side of the circular obstacle.

explained in full detail in [9], *versus* the foam velocity V for six different foam thicknesses (Fig. 9a). As usual, the drag increases with increasing foam velocity.

More importantly for this paper, at given velocity, and especially at the limit of vanishing velocity, the drag increases with increasing foam thickness. This is due to i) the decrease of liquid fraction with increasing foam thickness, as shown by the snapshots of the two extreme foam thicknesses in Figure 9a; ii) the increase in the height of the films with increasing foam thickness. We fit the data by the formula $F = F_Y^t + AV^a$ to get the values of the total yield drag F_Y^t for the various foam thicknesses.

Notably, for the smallest foam thickness ($h = 2.0\,\mathrm{mm}$) the foam is almost decompacted and the drag tends to vanish at low velocity. More precisely, the fit gives an unphysical negative value. This suggests that the rigidity loss transition [32] occurs for a foam thickness between 2.0 and 2.5 mm.

Appendix A.2. Comparison of network and total yield drags

We measure the line tension directly as the force exerted on the obstacle by a single soap film, as shown in
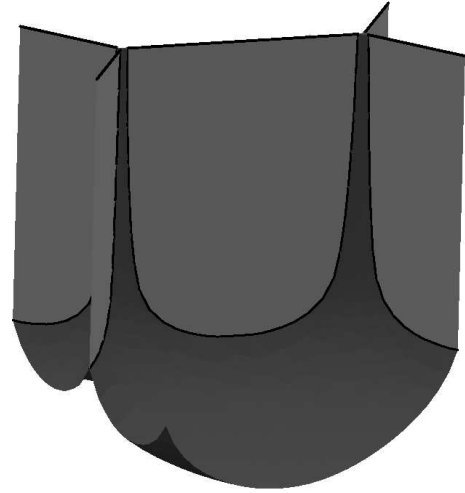

Fig. 10. Shape of the interfaces between bubbles, for bubbles of area $16.0\,\mathrm{mm}^2$ and volume $\mathcal{V} = 16.0 \times 3.5\,\mathrm{mm}^3$, calculated with the Surface Evolver. Vertical films are shown in light grey and the liquid surface in dark grey. To reproduce the experiment, we enforce the hexagonal symmetry and include the buoyancy. For simplicity, the junction between lateral faces and the top plate is assumed to be orthogonal.

Figure 9b, for two thicknesses. Its value is 0.44 mN for $h = 4.0\,\mathrm{mm}$, and 0.49 mN for $h = 4.5\,\mathrm{mm}$. This suggests that $\lambda/h \approx 110\,\mathrm{mN/m}$.

The actual gas-liquid interfaces have a 3D curvature to match tangentially the water surface and the glass plate (Fig. 10). This explains why the the measured value is between a lower bound, $\lambda/h = 2\gamma \approx 52\,\mathrm{mN/m}$ expected for a vertical soap film (that is, two flat gas/liquid interfaces), and an upper bound, $\lambda/h = (2+\pi)\gamma \approx 134\,\mathrm{mN/m}$, expected for two films with circular cross-section (see [39] for details).

Using the measured value of λ, we determine the absolute value of the network yield drag F_Y^n in experiments. We check (data not shown) that F_Y^n is consistently of the same order of magnitude, but lower than the value of F_Y^t measured directly. The remaining part is attributed to the pressure contribution F_Y^p, to be described in a further paper [34]. The spatial variation of bubble height h due to pressure differences is always less than 10%, giving an upper limit to the spatial variations of λ.

Appendix B. Variation of F_Y^n with the cut-off length

We consider here only the bubbles touching the obstacle, and the contribution of their walls to the yield drag. We assume that i) the foam is truly 2D and all bubbles have the same area (ideal 2D monodisperse foam); ii) pressure P is the same for each bubble, *i.e.* bubble walls are straight and all Plateau borders have the same radius of curvature R; iii) the obstacle is much larger than the bubbles ($\sqrt{A} \ll d_0$) so that we can neglect its curvature at the bubble
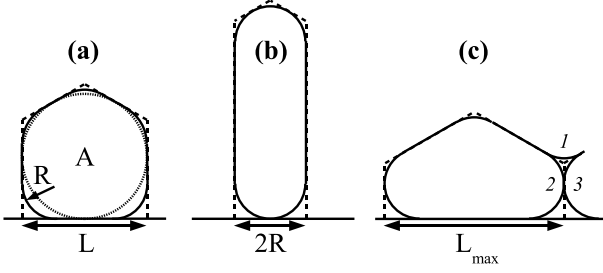
Fig. 11. Model configuration of the bubbles in contact with the obstacle. (a) Equilibrium configuration: the dashed line represents a polygonal bubble at $\Phi = 0$, the dotted line is a circular bubble at $\Phi = \Phi_c$, and the solid line represents the intermediate case $(0 < \Phi < \Phi_c)$, with straight edges and curved triangular vertices. (b) Configuration at the limit of detachment: two neighbouring vertices on the boundary of the obstacle come into contact. (c) Configuration at the point of attachment of a new bubble. There is one vertex between bubble 2, bubble 3 and the obstacle, and a second vertex between bubbles 1, 2 and 3. When these two vertices come into contact, bubble 1 attaches to the obstacle.

scale. This latter approximation could in principle affect the bubbles upstream, which share a long edge with the obstacle. However, it should not greatly affect the bubbles downstream, which are the main contributors to the drag.

Appendix B.1. Geometry

To model a wet foam, we apply the decoration theorem [32]: the liquid is present only at the vertices which decorate an ideally dry foam. For a bubble touching the obstacle, we denote by L the distance between two neighbouring vertices in contact with the obstacle (Fig. 11a).

When the foam flows, bubbles attach to the obstacle upstream, and detach from it downstream. Visual observation of both experiments (Fig. 1) and simulations (Fig. 2) indicate that bubbles are flattened along the obstacle at the leading side of the obstacle, and that they progressively stretch streamwise at the trailing side.

L reaches its minimum value downstream, where bubbles detach. There, two neighbouring (decorated) vertices come in contact, and L equals the cut-off length $2R$ (Fig. 11b).

On the other hand, for a new bubble to attach to the obstacle upstream, two bubbles must detach through the configuration of Figure 11c. In this case, a vertex between three bubbles merges with one between two bubbles and the wall. The cut-off length is different, and now equals $(1 + 1/\sqrt{3})R$. This geometrically determines that the maximum bubble width $L_{\max}$ obeys:

$$A = \left(1 + \frac{1}{\sqrt{3}}\right) RL_{\max} + \frac{L_{\max}^2}{4\sqrt{3}}. \qquad (B.1)$$

Inverting equation (B.1) yields $L_{\max}$:

$$L_{\max}(A, R) = 2\sqrt{(\sqrt{3}+1)^2 R^2 + A\sqrt{3}}$$
$$-2(\sqrt{3}+1)R. \qquad (B.2)$$

At low liquid fraction, $L_{\max}$ tends to a finite value, namely $\sqrt{4A\sqrt{3}}$; there is no singularity at vanishing R. Conversely, at high liquid fraction, $L_{\max}$ varies greatly with R, so it is preferable to rewrite equation (B.2) and determine R from the measurement of $L_{\max}$:

$$R(A, L_{\max}) = \left(1 + \frac{1}{\sqrt{3}}\right)^{-1} \left(\frac{A}{L_{\max}} - \frac{L_{\max}}{4\sqrt{3}}\right). \qquad (B.3)$$

Appendix B.2. Continuous assumption

We assume that the shape of the bubbles varies smoothly from the configuration of Figure 11c upstream to that of Figure 11b downstream: $2R < L < L_{\max}$. Since the obstacle is much larger than the bubbles, we switch from a discrete to a continuous description of the bubbles. We thus consider L as a continuous function of the ortho-radial angle θ along the obstacle boundary: $\theta = 0$ downstream, π (and $-\pi$) upstream. Equivalently, L^{-1} is the linear density of vertices along the obstacle boundary.

Then $L(0) = 2R$, $L(\pm\pi) = L_{\max}$. To interpolate between these values, we assume the following phenomenological dependence, reflecting that all bubbles in the range $|\theta| \geq \pi/2$ appear squashed against the obstacle:

$$|\theta| \leq \pi/2 : \quad L(\theta) = \left(R + \frac{1}{2}L_{\max}\right)$$
$$+ \left(R - \frac{1}{2}L_{\max}\right)\cos 2\theta, \qquad (B.4)$$
$$|\theta| \geq \pi/2 : \quad L(\theta) = L_{\max}.$$

Since each bubble edge exerts a pulling force of magnitude λ along the outward normal vector of the obstacle boundary, the network contribution to the drag is

$$F = \frac{\lambda d_0}{2} \int_{-\pi}^{\pi} \frac{\cos\theta}{L(\theta)} \, d\theta. \qquad (B.5)$$

To compute this integral, we introduce two dimensionless variables, both functions of A and R:

$$\varepsilon = \frac{R}{\sqrt{A}}, \qquad (B.6)$$

$$\beta = \frac{L_{\max}}{2R}. \qquad (B.7)$$

The physical meaning of ε is equivalent to the liquid fraction, since

$$\Phi = (2\sqrt{3} - \pi)\varepsilon^2. \qquad (B.8)$$

On the other hand, β quantifies the amount of up/downstream asymmetry, that is, the squashing and stretching of bubbles. It increases when Φ (or equivalently ε) decreases (Eq. (B.2)):

$$\beta(\Phi) = \sqrt{(\sqrt{3}+1)^2 + \frac{(6 - \sqrt{3}\pi)}{\Phi}} - (\sqrt{3}+1). \qquad (B.9)$$

When Φ goes to zero, ε goes to zero, too, and β diverges.

Using these variables, equation (B.5) yields

$$F = \frac{\lambda \, d_0}{L_{\max}} \left[\frac{\beta}{\sqrt{\beta - 1}} \arctan\left(\sqrt{\beta - 1}\right) - 1 \right]. \quad (B.10)$$

At high liquid fraction, the force F vanishes when $\beta = 1$, that is (Eq. (B.9)) when

$$\Phi = \frac{2\sqrt{3} - \pi}{2 + \sqrt{3}} = 0.086. \quad (B.11)$$

At low liquid fraction, we develop equation (B.10) to leading-order in β and insert the leading-order term of equation (B.9) to obtain equation (10).

References

1. R.G. Larson, *The Structure and Rheology of Complex Fluids* (Oxford University Press, New York, 1999).
2. A. Saint-Jalmes, D.J. Durian, J. Rheol. **43**, 1411 (1999).
3. D. Weaire, S. Hutzler, *The Physics of Foams* (Oxford University Press, Oxford, 1999).
4. R. Höhler, S. Cohen-Addad J. Phys.: Condens. Matter **17**, R1041 (2005).
5. D.M.A. Buzza, C.-Y. D. Lu, M.E. Cates, J. Phys. II **5**, 37 (1995).
6. F. Graner, Y. Jiang, E. Janiaud, C. Flament, Phys. Rev. E **63**, 11402 (2001).
7. H.M. Princen, J. Colloid. Interface Sci. **91**, 160 (1983).
8. S.A. Khan, R.C. Armstrong, J. Non-Newtonian Fluid Mech. **22**, 1 (1986).
9. B. Dollet, F. Elias, C. Quilliet, C. Raufaste, M. Aubouy, F. Graner, Phys. Rev. E **71**, 031403 (2005).
10. P.L.J. Zitha, Transp. Porous Media **52**, 1 (2003); S.J. Cox, S. Neethling, W.R. Rossen, W. Schleifenbaum, P. Schmidt-Wellenburg, J.J. Cilliers, Colloids Surf. A **245**, 143 (2004).
11. I. Cantat, N. Kern, R. Delannay Europhys. Lett. **65**, 726 (2004).
12. N.D. Denkov, S. Tcholakova, K. Golemanov, V. Subramanian, A. Lips, Colloids Surf. A **282-283**, 329 (2006).
13. Workshop on Foam Rheology In Two dimensions (FRIT), Aberystwyth (UK), June 2005, `http://users.aber.ac.uk/sxc/frit.html`.
14. M. Asipauskas, J.A. Glazier, unpublished.
15. S.J. Cox, M.D. Alonso, S. Hutzler, D. Weaire, in *Eurofoam 2000, Proceedings of the 3rd Euroconference on Foams, Emulsions and Applications, Delft (The Netherlands), June 2000*, edited by P. Zitha, J. Banhart, G. Verbist (MIT Verlag, Bremen, 2000) pp. 282-289.
16. J.R. de Bruyn, Rheol. Acta **44**, 150 (2004).
17. I. Cantat, O. Pitois, J. Phys.: Condens. Matter **17**, S3455 (2005).
18. I. Cantat, O. Pitois, Phys. Fluids **18**, 083302 (2006).
19. M.F. Vaz, S.J. Cox, Philos. Mag. Lett. **85**, 415 (2005).
20. E. Janiaud, D. Weaire, S. Hutzler, to be published in Colloids. Surf. A (2007).
21. This is due to the left-right symmetry of a bubble wall meeting the solid boundary. This is independent of the hydrophilic or hydrophobic nature of the solid surface (which would only play a role, through the presence or absence of a wetting film, in the energy dissipation, not relevant in the present paper).
22. A.D. Gopal, D.J. Durian, Phys. Rev. Lett. **91**, 188303 (2003).
23. S. Cohen-Addad, R. Höhler, Y. Khidas, Phys. Rev. Lett. **93**, 028302 (2004).
24. B. Dollet, F. Elias, C. Quilliet, A. Huillier, M. Aubouy, F. Graner, Colloids. Surf. A **263**, 101 (2005).
25. K. Brakke, Exp. Math. **1**, 141 (1992).
26. S.J. Cox, B. Dollet, F. Graner, Rheol. Acta **45**, 403 (2006).
27. J. Lauridsen, M. Twardos, M. Dennin, Phys. Rev. Lett. **89**, 098303 (2002).
28. M. Twardos, M. Dennin, Phys. Rev. E. **71**, 061401 (2005).
29. Y. Jiang, P.J. Swart, A. Saxena, M. Asipauskas, J.A. Glazier, Phys. Rev. E **59**, 5819 (1999).
30. D.J. Srolovitz, M.P. Anderson, G.S. Grest, P.S. Sahni, Scr. Metall. **17**, 241 (1983).
31. E.A. Holm, J.A. Glazier, D.J. Srolovitz, G.S. Grest, Phys. Rev. A **43**, 2662 (1991).
32. F. Bolton, D. Weaire, Phys. Rev. Lett. **65**, 3449 (1990).
33. S.J. Cox, D. Weaire, M.F. Vaz, Eur. Phys. J. E **7**, 311 (2002).
34. B. Dollet, F. Graner, to be published in J. Fluid. Mech. (2007) physics/0606170.
35. B. Dollet, M. Durth, F. Graner, Phys. Rev. E **73**, 061404 (2006).
36. H.M. Princen, A.D. Kiss, J. Colloid Interface Sci. **128**, 176 (1989).
37. E. Janiaud, D. Weaire, S. Hutzler, Phys. Rev. Lett. **97**, 038302 (2006).
38. Y. Wang, K. Krishan, M. Dennin, Phys. Rev. E **73**, 031401 (2006).
39. B. Dollet, *Écoulement bidimensionnels de mousse autour d'obstacles*, PhD Thesis, unpublished, available online at `http://www-lsp.ujf-grenoble.fr/pdf/theses/dtbn.pdf`.